nature photonics

ARTICLES

PUBLISHED ONLINE: 3 AUGUST 2015 | DOI: 10.1038/NPHOTON.2015.132

Direct optical nanoscopy with axially localized detection

N. Bourg[1,2], C. Mayet[2], G. Dupuis[2], T. Barroca[3], P. Bon[3], S. Lécart[2], E. Fort[3] and S. Lévêque-Fort[1,2]*

Evanescent light excitation is widely used in super-resolution fluorescence microscopy to confine light and reduce background noise. Here, we propose a method of exploiting evanescent light in the context of emission. When a fluorophore is located in close proximity to a medium with a higher refractive index, its near-field component is converted into light that propagates beyond the critical angle. This so-called supercritical-angle fluorescence can be captured using a high-numerical-aperture objective and used to determine the axial position of the fluorophore with nanometre precision. We introduce a new technique for three-dimensional nanoscopy that combines direct stochastic optical reconstruction microscopy (dSTORM) with dedicated detection of supercritical-angle fluorescence emission. We demonstrate that our approach of direct optical nanoscopy with axially localized detection (DONALD) typically yields an isotropic three-dimensional localization precision of 20 nm within an axial range of ~150 nm above the coverslip.

Single-molecule localization microscopies (SMLMs) such as fluorescence photoactivated localization microscopy ((F)PALM) and direct stochastic optical reconstruction microscopy (dSTORM) have shattered the spatial resolution barrier imposed by the diffraction limit. These techniques are based on the sequential detection of several thousands of individual fluorescent molecules[1–4]. In their simplest implementations, these methods typically improve the lateral resolution by one order of magnitude, but their axial resolution is still limited by diffraction. Specific techniques must be developed to tackle this strong anisotropic resolution which compromises three-dimensional imaging. Super-localization techniques must be combined with point spread function (PSF) engineering methods to measure the depth position of each detected fluorophore[5–9]. Single[5] and double[7] cylindrical-lens methods have achieved axial localization precisions of 22 and 8 nm, respectively. The former is very stable and straightforward to implement, whereas the higher precision of the latter comes at the cost of increased complexity. Similarly, alternative elaborate methods such as interferometric PALM (iPALM)[10] and self-bending PSF (SB-PSF)[11] can achieve axial localization precisions of 4 and 15 nm, respectively[12]. All these strategies provide only the relative axial positions of the fluorophores with respect to an arbitrary focal plane. Hence, three-dimensional optical nanoscopy is in need of a method that combines high localization precision, simplicity of implementation and absolute axial positioning.

Here, we report a new approach termed 'direct optical nanoscopy with axially localized detection' (DONALD). This type of nanoscopy combines a standard super-localization technique with supercritical-angle fluorescence (SAF) analysis[13]. The latter is based on the light emission above the critical angle that occurs when fluorophores are placed in the vicinity of the coverslip interface. Within this region, DONALD achieves three-dimensional nanometre resolution, yielding the absolute axial position of the fluorophores with a precision down to 15 nm.

Principle

A fluorophore can be modelled as a dipolar emitter radiating in the far field. This dipole is also endowed with a non-propagative near-field component that depends on the surrounding refractive index n_m. In the presence of an interface with a medium with a refractive index of $n_g > n_m$ (where m indicates the medium and g indicates the glass interface), the transmitted light follows the Snell–Descartes law of refraction (Fig. 1a). The refracted light is emitted within a cone that is limited by the critical angle $\theta_c = \arcsin(n_m/n_g)$. This component is referred to as under-critical angle fluorescence (UAF). However, if the fluorophore–interface distance d is smaller than the fluorescence wavelength λ_{em}, then additional SAF emission is observed. The evanescent near-field component in the homogeneous medium surrounding the fluorophores, with an index of refraction of n_m, becomes propagative beyond the critical angle θ_c inside the medium of higher refractive index, $n_g > n_m$. SAF emission can be detected for fluorophores in the cellular medium located in the vicinity of the coverslip. The SAF intensity is potentially equal to as much as 50% of all fluorescence emitted into the coverslip when the fluorophore is in direct contact with the interface ($d = 0$) (Fig. 1b)[14].

The number of UAF photons N^{UAF} remains nearly constant as a function of the interface–fluorophore distance d, but the number of SAF photons N^{SAF} decreases approximately exponentially[15]. Hence, the simultaneous measurement of N^{SAF} and N^{UAF} and computation of the fluorophore SAF ratio $\rho^{SAF} = N^{SAF}/N^{UAF}$ for each detected fluorophore can be used to determine the absolute axial position of the fluorophore, d. Here, we propose that this principle may be used to achieve axial localization with nanometre precision. Ruckstuhl and colleagues have already successfully applied this principle using a home-made parabolic objective[15,16]. Unfortunately, this point scanning objective is not compatible with lateral super-localization. Current commercial high-numerical-aperture (NA) objectives (NA $\approx n_g > n_m$) allow the efficient collection of SAF emission[17]. The angular distributions of both the SAF and UAF components can be directly observed in their back-focal plane (BFP). These aplanetic objectives satisfy the Abbe sine relation: light emitted with an angle θ lies within a circle of radius $\rho = n_g f \sin\theta$ in the BFP, where n_g is the refractive index of the immersion medium (chosen to match the refractive index of the

[1]Institut des Sciences Moléculaires d'Orsay (ISMO), Université Paris-Sud, CNRS UMR 8214, Orsay Cedex F91405, France. [2]Université Paris-Sud, Centre de Photonique BioMédicale (CPBM), Fédération LUMAT, CNRS FR 2764, Orsay Cedex F91405, France. [3]Institut Langevin, ESPCI ParisTech, CNRS, PSL Research University, 1 rue Jussieu, F-75005 Paris, France. *e-mail: sandrine.leveque-fort@u-psud.fr

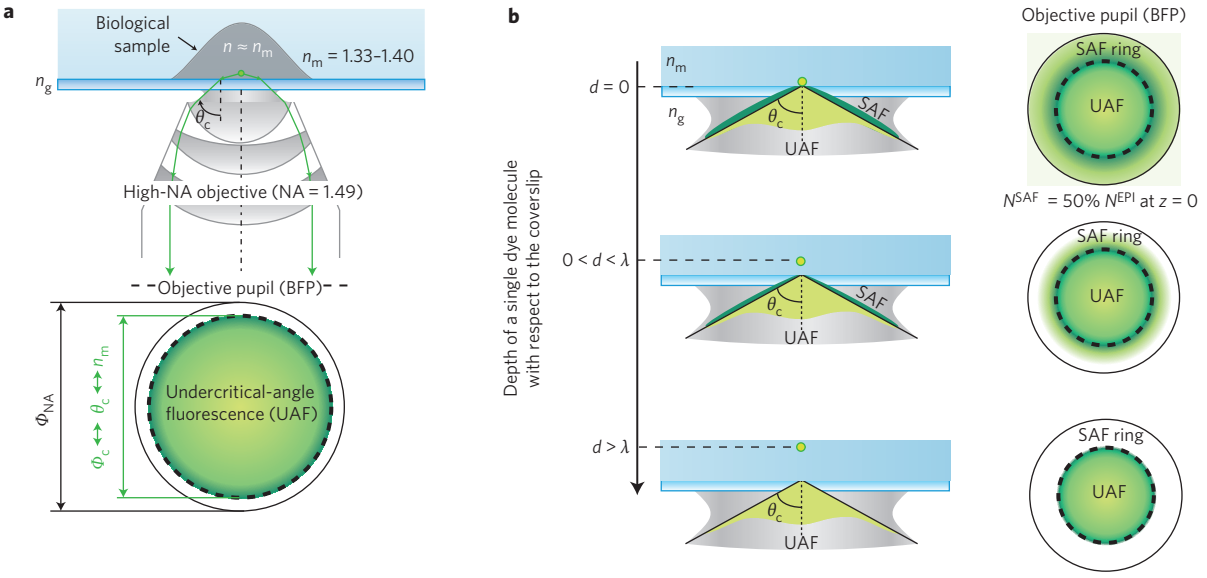

Figure 1 | Far- and near-field emission components. a, The far-field emission component (UAF) has an angular distribution determined by the law of refraction and limited by the critical angle θ_c. This angular distribution of light can be retrieved on the BFP within a plane disk of diameter Φ_c, which is related to θ_c. **b**, A position of the near-field component (SAF) of a dye molecule located in the near-field region (0 to λ_{em}) is collected by the objective beyond θ_c. The number of SAF photons, N^{SAF}, is potentially equal to as much as 50% of N^{EPI} when the dye is in close proximity to the coverslip and decreases exponentially as the dye depth d increases.

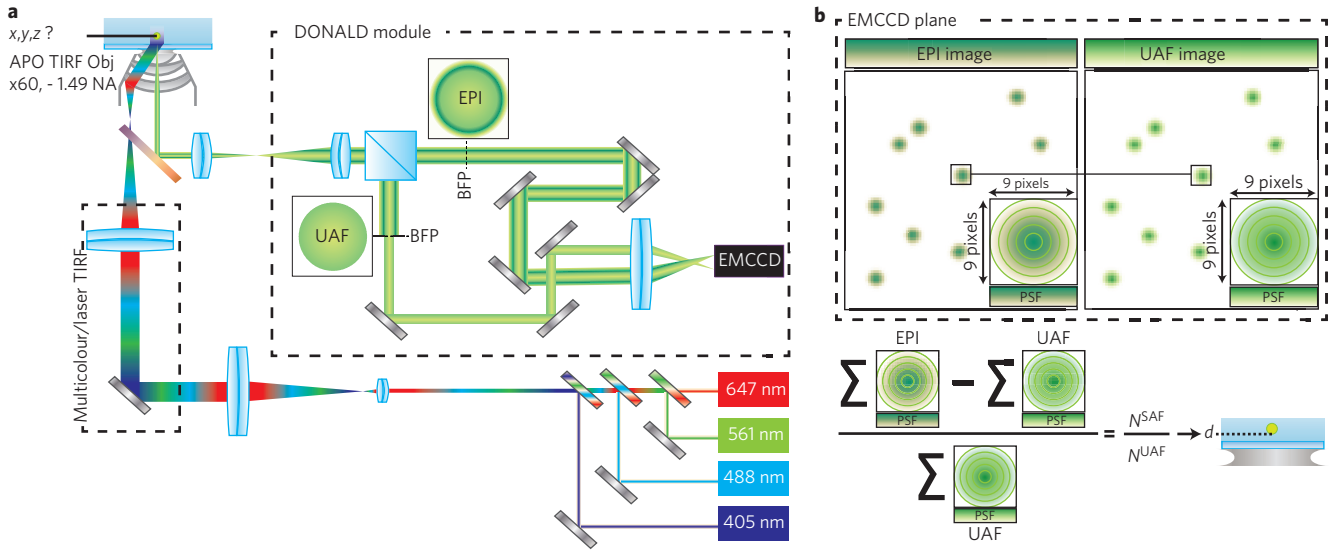

Figure 2 | Direct optical nanoscopy with axially localized detection. a, Schematic of the experimental set-up. A homemade multicolour/laser TIRF stage is connected to the input of a conventional wide-field microscope. TIRF excitation light passes through a four-colour filter set (405, 488, 561, 647 nm) and an apochromatic TIRF objective with NA = 1.49. The fluorescence emission of dye molecules is collected by the objective and reflected to the DONALD module, which splits the fluorescence into two parts. The EPI part is directly imaged on one half of an EMCCD, and the UAF part (the SAF component is blocked in the BFP) is recorded on the other half. **b**, DONALD data analysis. First, in the UAF and EPI portions of the frame, each PSF is super-localized in two dimensions and the number of UAF and EPI photons (N^{UAF} and N^{EPI}, respectively) are calculated via signal integration in a 9 × 9 area of pixels. Finally, the SAF ratio is computed and converted into the absolute dye depth d.

glass coverslip) and f is the focal length of the objective. Hence, the UAF emission lies within a disk of radius $n_g f \sin\theta_c$ and the SAF component has a ring shape and surrounds the UAF disk up to a radius of fNA (Fig. 1b).

Various strategies can be implemented to discriminate between the UAF and SAF components in the BFP. A straightforward method of selecting for SAF emission consists of using a disk-shaped mask in the BFP to block the UAF emission. The diameter of the resulting PSF, σ_{PSF}^{SAF}, is 1.7 times larger than that of the standard PSF[17], and N^{SAF} represents less than 50% of the total number of collected photons, N^{EPI} (where EPI indicates epifluorescence and $N^{EPI} = N^{UAF} + N^{SAF}$). However, this strategy causes degradation of the lateral two-dimensional localization precision σ because in SMLM, $\sigma \propto \sigma_{PSF}/\sqrt{N}$ (ref. 18). The detection of SAF emission for enhanced axial localization should not come at the cost of a degradation in lateral resolution. Our alternative approach extracts N_{SAF} by measuring N_{EPI} and N_{UAF} on two simultaneously acquired PSFs. Both PSFs are well defined, with a significant

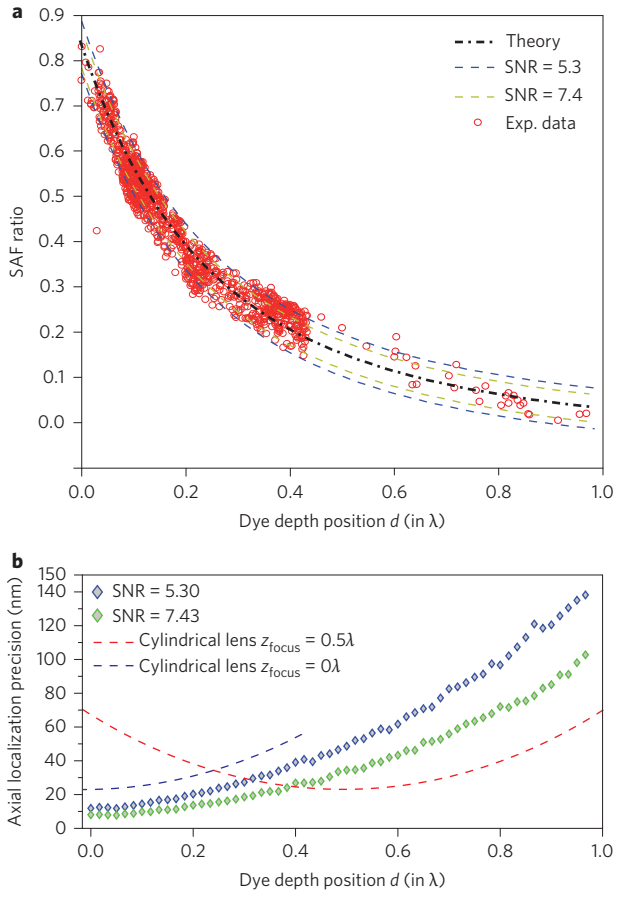

Figure 3 | DONALD theory. a, Theoretical decay of the SAF ratio (black line) as a function of dye depth d for $n_m = 1.33$ and $n_g = 1.515$. A total of 5,000 iterations of a Monte Carlo simulation of this theory were performed for two different SNRs: 5.30 (blue error line) and 7.43 (green error line). **b**, Monte Carlo simulations were used to calculate the axial localization precision for both SNRs. The localization precisions of the single cylindrical lens for two extreme focal plane positions are represented using a model extracted from ref. 23. Experimental verification of the theory was performed using 20 nm red beads embedded in 3% agarose gel ($n_m = 1.33$). The DONALD module was used to measure the SAF ratio and a PSF shaping method (cylindrical lens) was applied to determine the depth. The experimental results (**a**, red circles) are consistent with and confirm the DONALD theory.

number of photons, and can thus be used to compute the lateral two-dimensional super-localization with a good signal-to-noise ratio (SNR). By simultaneously capturing N^{EPI} and N^{UAF}, we can determine $N^{SAF} = N^{EPI} - N^{UAF}$. Notably, this approach is the single-molecule analogue of the full-field virtual SAF technique[19,20]. Finally, by computing ρ^{SAF}, we achieve axial super-localization of the fluorophore.

Experimental set-up

The experimental set-up consists of a home-made DONALD module inserted between the output of a standard full-field microscope and an electron-multiplying charge-coupled device (EMCCD) camera. This module uses a beamsplitter to split the fluorescence emission into two imaging paths (Fig. 2a). The first EPI path is directly imaged onto half of the EMCCD detector and is used to compute N^{EPI} for a given PSF. In the second path, the SAF ring is blocked out in the image plane of the objective BFP in order to generate a corresponding UAF-only PSF on the other half of the EMCCD detector. N^{UAF} is computed from this image. When a fluorophore is imaged on both paths, it is first super-localized in two dimensions using a wavelet segmentation algorithm[21]. N^{EPI} and N^{UAF} are then measured via numerical integration within a PSF region of 9×9 pixels. ρ^{SAF} (d) is then computed to determine the depth d of the fluorophore (Fig. 2b and Supplementary Fig. 1). The precision of axial localization depends on n_m, n_g and the SNR, which is defined as $SNR = I^{EPI}_{max}/\sqrt{2\pi I^{EPI}_{max}}$, where I^{EPI}_{max} is the maximum intensity of the EPI PSF[21]. We performed Monte Carlo simulations of ρ^{SAF} as a function of d (with $0 < d < \lambda_{em}$) for our typical experimental conditions ($n_m = 1.33$, $n_g = 1.515$, SNR = 5.3 or 7.4)[22] (Fig. 3a and Supplementary Fig. 2). We then determined the axial localization precision, which decreases with increasing axial position of the fluorophore, d (see Fig. 3b and Supplementary Fig. 2 for more details regarding the simulations). For a typical SNR of 7.4, we found that the axial localization precision is better than 20 nm when $0 < d < 0.2\lambda_{em}$, and better than 40 nm when $0.2\lambda_{em} < d < 0.5\lambda_{em}$. As a comparison we plotted the axial localization precision of single cylindrical lens (model extracted from ref. 23) for two extreme positions of the focal plane relatively to the coverslip surface (0 and 0.5λ). For a more usual focal plane position (0.5λ), DONALD will offer higher performances of up to 0.4λ (Supplementary Fig. 3b,c). We performed several experiments to characterize DONALD localization precisions (see Supplementary Methods). We imaged a photoswitchable dye (such as CellMask Deep Red) immobilized at the coverslip and obtained an axial localization of $d = 0.5$ nm with a precision of $\sigma_d = 15.9$ nm (cf. Fig. 6c). We also repetitively imaged 20 nm fluorescent nanospheres directly deposited on a glass coverslip, in experimental conditions yielding a SNR similar to standard SMLM imaging[24] (Supplementary Fig. 3a). We used the ρ^{SAF} to localize the 20 nm nanospheres at their centre of mass. We measured an axial position of $d = 9.9$ nm with a precision of $\sigma_d = 15.2$ nm. To confirm the axial localization deduced from ρ^{SAF} for an initially unknown three-dimensional sample, we used 20 nm fluorescent nanospheres embedded in a 3% agarose gel ($n_m = n_{water} = 1.33$) deposited on a coverslip ($n_g = 1.515$). For each bead, we measured both the ρ^{SAF} with the DONALD module and the depth d using the cylindrical lens method, which determines the axial position d from the PSF shape[5]. The experimental results and theoretical calculations were in excellent agreement (red circles and black line, respectively, Fig. 3a). The theory can thus be used directly to convert a measured ρ^{SAF} value into the absolute axial position of the fluorophore.

Results

We demonstrated the performance of DONALD in cell imaging. We first imaged dSTORM frames of F-actin labelled with phalloidin-Alexa 488 of CHO cells immersed in a thiol + oxygen scavenger buffer (Supplementary Methods) with a refractive index of $n_m = 1.345$ (ref. 4, Fig. 4a,b). Fluorophore excitation was achieved using a blue laser ($\lambda_{exc} = 488$ nm) in total internal reflection fluorescence (TIRF) configuration. The laser power was held constant throughout the entire imaging process (2 kW cm^{-2}). The number of detected molecules in each frame remained stable throughout the entire acquisition (15,000 frames) by virtue of the amino acid residue tryptophan, which is a component of the actin probe phalloidin. Tryptophan quenches rhodamine dyes such as Alexa Fluor 488[25]. The number of photons was typically around 4,230 with 779,149 detected molecules. Using the DONALD technique, we achieved an axial resolution of 35 ± 1 nm for structures located ~105 nm away from the coverslip (Fig. 4b,c,e: zones 1 and 3). Typical transverse profiles of actin filaments are presented in Fig. 4d. For filaments located at $d \approx 180$ and $d \approx 148$ nm, we measured axial resolutions of 62 and 54 nm, respectively (Fig. 4a,c,e: zones 2 and 4). Other actin-filament profiles are presented in Supplementary Fig. 6. As expected from the model, the closer to the coverslip these features were located, the better the axial resolution.

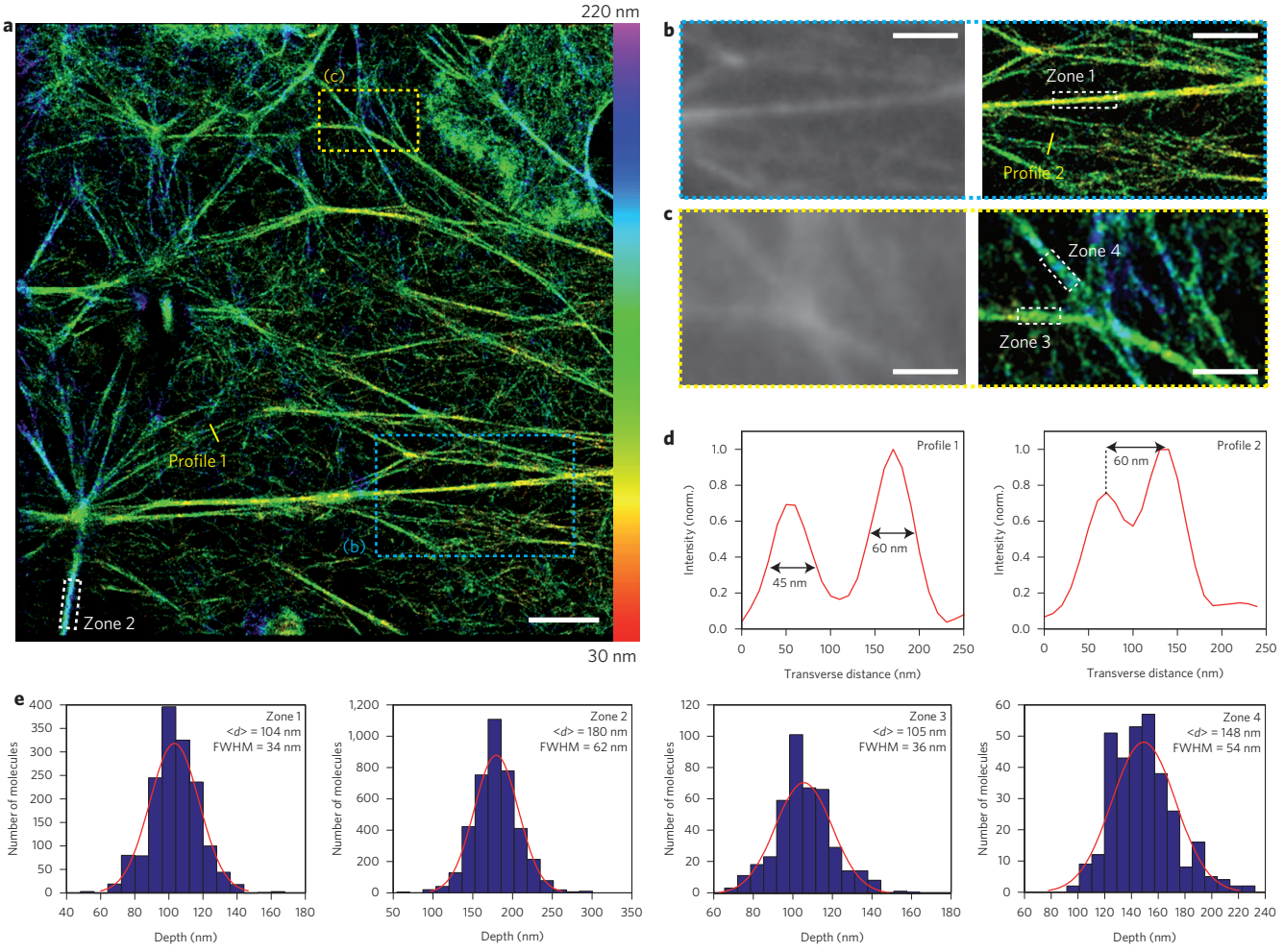

Figure 4 | dSTORM imaging of F-actin in CHO cells immersed in a thiol + oxygen scavenger buffer using DONALD. a, Three-dimensional DONALD image in which the depth is colour-coded as indicated by the coloured depth scale bar. **b**,**c**, Diffraction-limited (left) and three-dimensional (right) images of sub-areas of **a**, indicated by the blue and yellow boxes. **d**, Transverse profiles of 'Profile 1' and 'Profile 2' in **a** and **b**. **e**, Axial profiles of various structures (zones 1–4) in **a** and **b**. Axial resolutions of 34–36, 54 and 62 nm were achieved for filaments located at depths of 104–105, 148 and 180 nm, respectively. Scale bars, 3 μm (**a**), 2 μm (**b**), 1 μm (**c**).

We next imaged, with TIRF excitation, the microtubule network of COS-7 cells labelled with antibody–Alexa 647 and immersed in a similar thiol + oxygen scavenger buffer (typical photon rate of ~7,877, with 851,662 detected molecules). Diffraction-limited TIRF and three-dimensional false-colour DONALD images are shown in Fig. 5a and b, respectively. For a microtubule located at ~36 nm from the coverslip (Fig. 5b,d,e), an estimated value of 53.5 nm was obtained for the diameter, as expected due to the additional size of the primary and secondary antibodies[11]. For microtubules located at $d \approx 63$ and 118 nm, we measured axial resolutions of 56.2 and 80.4 nm, respectively (Fig. 5c,e). Nice evidence of the system localization precision is given by its ability to resolve the microtubule hollowness, which is not straightforward as it depends on several factors including labelling density, environment and localization precision. The labelled antibodies are expected to form a ring around the microtubule with an inner diameter of ~25 nm and an outer diameter of ~60 nm, as observed in electron microscopy[26]. Projected along the axial or lateral direction, the labelling density presents two peaks separated by ~60 nm. When observed with a Gaussian localization precision, the measured peak distance should decrease with localization precision (Supplementary Fig. 7a). Indeed, DONALD permits the resolution of the lateral hollowness of a microtubule located close to the surface ($d \approx 35$ nm), with a peak distance of 33 ± 2 nm (Fig. 5b,f). The axial hollowness can also be evidenced, but with a lower peak distance of 22 ± 5 nm as $\sigma_d > \sigma_x$. This axial peak distance can thus be used to confirm the axial localization precision of ~15.5 nm (Supplementary Fig. 7b).

As supercritical emission can be detected for fluorophores axially located up to nearly a wavelength above the interface, DONALD can also be used to localize deeper into the sample using a highly inclined beam to preserve a low background. Microtubules positioned at $d \approx 550$ nm (indicated by an arrow in Supplementary Fig. 4a,b), undetected in the TIRF image (Supplementary Fig. 4a), can be detected in the DONALD image (Supplementary Fig. 4b), although with a lower axial localization precision.

An alternative buffer based on Vectashield associated with Alexa 647 (ref. 27) can be used in conjunction with DONALD (Supplementary Fig. 5). However, it gives slightly poorer performances, for two reasons. First, the higher refractive index of the Vectashield-based buffer ($n_m = 1.38$ compared with 1.345 for the thiol-based buffer) causes the critical angle to be higher, thus lowering the SAF ratio for a given objective. Second, in our case, the long-term efficiency of the Vectashield-based buffer was not as good as that of the thiol-based buffer, hence limiting the number of frames that could be acquired with an acceptable detection density (typically 2,500 versus 15,000).

Probing the cell–surface distance with nanometric resolution opens a new way to quantify cell adhesion and motility, which are

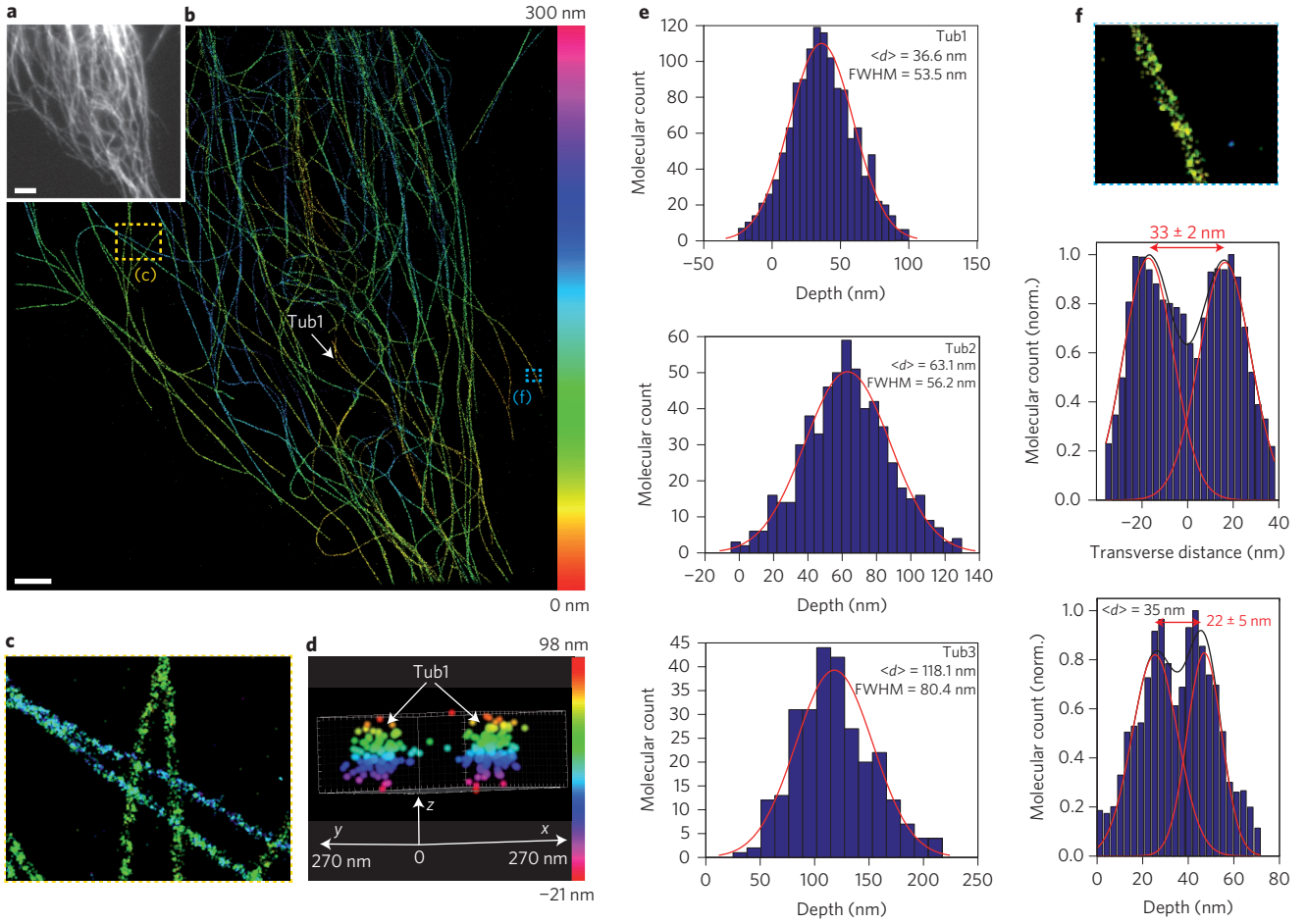

Figure 5 | dSTORM imaging of microtubules immersed in a thiol + oxygen scavenger-based buffer using DONALD. a, Diffraction-limited image of the microtubule network of immunofluorescently labelled COS-7 cells. **b**, Three-dimensional super-resolved image of the same region shown in **a**, colour-coded as indicated by the coloured depth scale bar. **c**, Close-up of a microtubule indicated by the small yellow-boxed region in **b**. **d**, *x*–*z* plane of tubuline Tub1 produced using ViSP software. **e**, Axial profiles of three different microtubules shown in **b** and **c**. Axial resolutions of 53.5, 56.2 and 80.4 nm were obtained for filaments located at depths of depths of 36.6, 63.1 and 118.1 nm, respectively. **f**, Close-up of a microtubule located at a depth of 35 nm and indicated by the white arrow in **b**. Transversal and axial profiles of this microtubule are fitted with a double Gaussian. Transversal and axial hollowness values of 33 ± 2 and 22 ± 5 nm are measured, respectively. Scale bars, 1.5 μm (**a**), 3 μm (**b**), 240 nm (**c**), 190 nm (**f**).

key phenomenon in cell migration. A recent approach based on fluorescence lifetime variations of the dye depending on its position relative to a plasmonics substrate was implemented to probe membrane elevation. Of particular interest is the demonstration of great differences in the cell–interface distance between a normal epithelial cell and cancerous cell lines[28]. This approach only provides nanometric axial resolution, while retaining conventional *xy* resolution. DONALD could nicely complement this approach by giving access to isotropic local membrane variation at the cost of less accurate *z* localization. We demonstrate this capability on COS-7 cells labelled with a membrane-staining fluorophore (CellMask Deep Red, Invitrogen) that is compatible with SMLM imaging (Fig. 6a). Localization information given by DONALD is converted into a three-dimensional view of the plasma membrane nanotomography (Fig. 6b), and local elevation along the filopodia can be extracted (Fig. 6d).

Discussion

In summary, DONALD is a new three-dimensional super-localization nanoscopy technique based on the detection of the near-field supercritical emission (SAF). The achieved precision of axial localization reaches 20 nm within the 150 nm nearest to the coverslip, with a lateral localization precision of 10 nm. For axial distances between ~180 and ~300 nm from the coverslip, the DONALD localization precision is at least equivalent to that achieved using current PSF engineering methods (~20–25 nm). However, a unique feature offered by DONALD is the access to the absolute depth of the fluorophore relatively to the coverslip. The localization of multiple proteins can thus be directly combined to reconstruct a complex three-dimensional biological architecture such as the focal adhesions or podosomes involved in cell migration, differentiation and proliferation[29]. Furthermore, recent developments have been proposed to sequentially image multiple target using a single fluorophore[30–32]. As it involves successive permanent or transient labelling with the fluorophore, accessing absolute localization will permit a straightforward axial reconstruction.

DONALD is not sensitive to local thickness variations and/or the tilt of the coverslip. In addition, whereas PSF engineering techniques are limited to a low concentration of fluorophores because of the enlargement of the PSF volume and hence tend to require the use of high laser power, DONALD can maintain the imaging speed of a standard two-dimensional super-localization microscope.

According to our simulations, an axial localization precision of 5–10 nm should be achievable, and improvements in DONALD localization efficiency are limited by the SNR. The same limitations, common to others SMLM techniques, will govern the performances

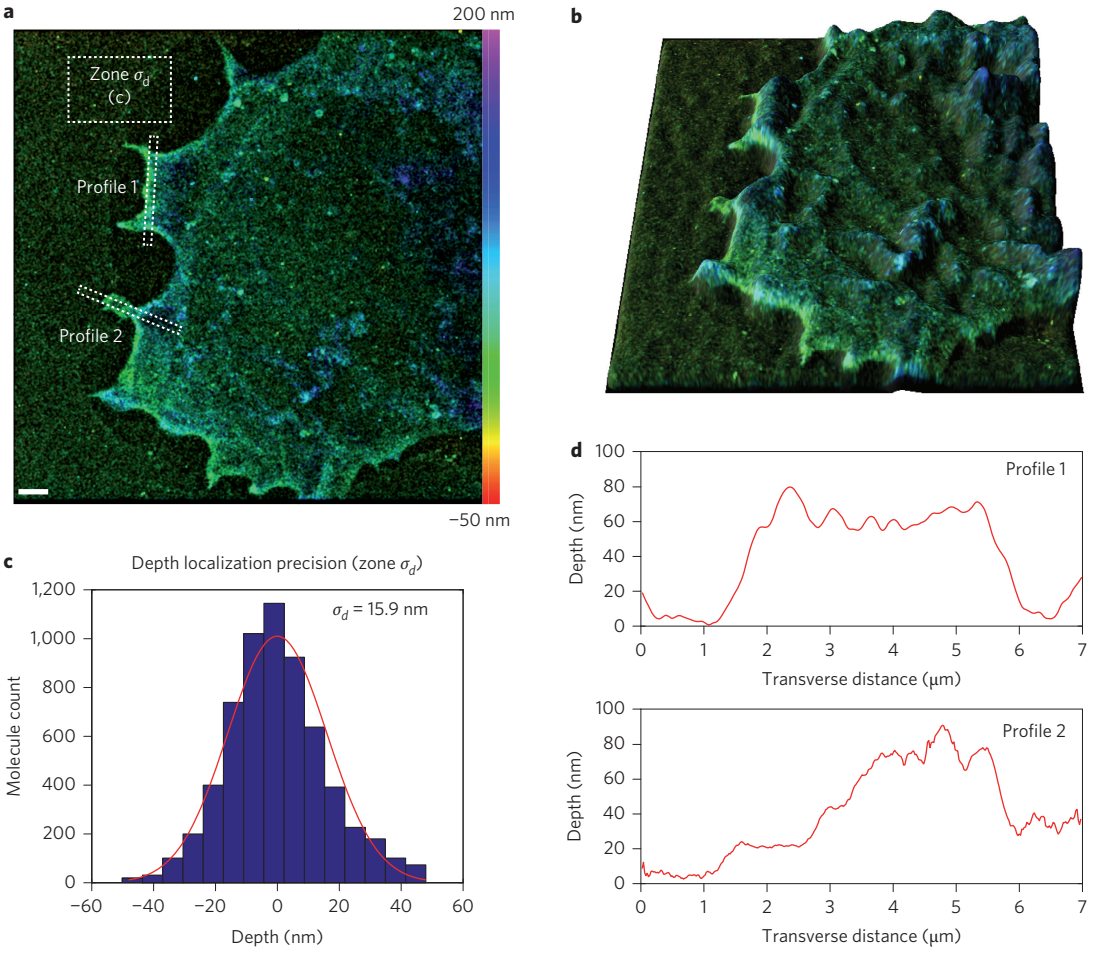

Figure 6 | SMLM imaging of plasma membrane immersed in a thiol + oxygen scavenger-based buffer using DONALD. a, Three-dimensional super-resolved image of the plasma membrane in COS-7 cells, colour-coded as indicated by the coloured depth scale bar. **b**, Three-dimensional visualization of the membrane nanotopography using ImageJ3D, with the same colour coding as in **a**. **c**, Axial localization precision measured from the dye molecules immobilized at the surface of the coverslip (zone σ_d in **a**: axial localization $d = 0.5$ nm with precision $\sigma_d = 15.9$ nm). **d**, Transverse profiles of 'Profile 1' and 'Profile 2' in **a**. Scale bar, 1.5 μm (**a**).

of DONALD in live-cell imaging. In single particle tracking PALM (SPT-PALM), a SNR close to 5.3 (ref. 21) is obtained with photo-convertible red fluorescent protein tdEosFP, which would only slightly decrease the localization compared to organic dyes (cf. Fig. 3b). Thanks to the rapid development of brighter proteins[33], alternative dyes[34] and new tag strategies[35], super-resolution imaging of dynamic components in living systems will benefit from increased localization performances. The rotational mobility of a fluorophore can be affected in the compartments of cells, and a constraint dipole can thus lead to a localization error[36]. A polarization-sensitive version of DONALD would be straightforward to implement by using an initial polarization beamsplitter. In a complementary manner, higher-NA objectives with NAs up to 1.65 or 1.70 could allow an increase in the SNR through enhancement of the SAF emission, thereby further improving the axial localization precision. Thanks to its simple and robust design, DONALD can be easily associated with existing SMLM set-ups while preserving a high photon detection efficiency.

Methods

Methods and any associated references are available in the online version of the paper.

Received 2 October 2014; accepted 1 July 2015; published online 3 August 2015

References

1. Betzig, E. *et al.* Imaging intracellular fluorescent proteins at nanometer resolution. *Science* **313,** 1642–1645 (2006).
2. Hess, S. T., Girirajan, T. P. K. & Mason, M. D. Ultra-high resolution imaging by fluorescence photoactivation localization microscopy. *Biophys. J.* **91,** 4258–4272 (2006).
3. Rust, M. J., Bates, M. & Zhuang, X. Stochastic optical reconstruction microscopy (STORM) provides sub-diffraction-limit image resolution. *Nature Methods* **3,** 793–795 (2006).
4. van de Linde, S. *et al.* Direct stochastic optical reconstruction microscopy with standard fluorescent probes. *Nature Protoc.* **6,** 991–1009 (2011).
5. Huang, B., Wang, W., Bates, M. & Zhuang, X. Three-dimensional super-resolution imaging by stochastic optical reconstruction microscopy. *Science* **319,** 810–813 (2008).
6. Izeddin, I. *et al.* PSF shaping using adaptive optics for three-dimensional single-molecule super-resolution imaging and tracking. *Opt. Express* **20,** 4957–4967 (2012).
7. Xu, K., Babcock, H. P. & Zhuang, X. Dual-objective STORM reveals three-dimensional filament organization in the actin cytoskeleton. *Nature Methods* **9,** 185–188 (2012).
8. Pavani, S. R. P. *et al.* Imaging beyond the diffraction limit by using a double-helix point spread function. *Proc. Natl Acad. Sci. USA* **106,** 2995–2999 (2009).
9. Badieirostami, M., Lew, M. D., Thompson, M. A. & Moerner, W. E. Three-dimensional localization precision of the double-helix point spread function versus astigmatism and biplane. *Appl. Phys. Lett.* **97,** 161103 (2010).
10. Shtengel, G. *et al.* Interferometric fluorescent super-resolution microscopy resolves 3D cellular ultrastructure. *Proc. Natl Acad. Sci. USA* **106,** 3125–3130 (2009).

11. Jia, S., Vaughan, J. C. & Zhuang, X. Isotropic three-dimensional super-resolution imaging with a self-bending point spread function. *Nature Photon.* **8,** 302–306 (2014).
12. Klein, T., Proppert, S. & Sauer, M. Eight years of single-molecule localization microscopy. *Histochem. Cell Biol.* **141,** 561–575 (2014).
13. Ruckstuhl, T., Enderlein, J., Jung, S. & Seeger, S. Forbidden light detection from single molecules. *Anal. Chem.* **72,** 2117–2123 (2000).
14. Fort, E. & Grésillon, S. Surface enhanced fluorescence. *J. Phys. D* **41,** 013001 (2008).
15. Ruckstuhl, T., Rankl, M. & Seeger, S. Highly sensitive biosensing using a supercritical angle fluorescence (SAF) instrument. *Biosens. Bioelectron.* **18,** 1193–1199 (2003).
16. Winterflood, C., Ruckstuhl, T., Verdes, D. & Seeger, S. Nanometer axial resolution by three-dimensional supercritical angle fluorescence microscopy. *Phys. Rev. Lett.* **105,** 108103 (2010).
17. Barroca, T., Balaa, K., Delahaye, J., Lévêque-Fort, S. & Fort, E. Full-field supercritical angle fluorescence microscopy for live cell imaging. *Opt. Lett.* **36,** 3051–3053 (2011).
18. Thompson, R. E., Larson, D. R. & Webb, W. W. Precise nanometer localization analysis for individual fluorescent probes. *Biophys. J.* **82,** 2775–2783 (2002).
19. Barroca, T., Balaa, K., Lévêque-Fort, S. & Fort, E. Full-field near-field optical microscope for cell imaging. *Phys. Rev. Lett.* **108,** 218101 (2012).
20. Barroca, T., Bon, P., Lévêque-Fort, S. & Fort, E. Supercritical self-interference fluorescence microscopy for full-field membrane imaging. *Proc. SPIE* **8589,** 858911 (2013).
21. Izeddin, I. *et al.* Wavelet analysis for single molecule localization microscopy. *Opt. Express* **20,** 2081–2095 (2012).
22. Tang, W. T., Chung, E., Kim, Y. H., So, P. T. C. & Sheppard, C. J. R. Investigation of the point spread function of surface plasmon-coupled emission microscopy. *Opt. Express* **15,** 4634–4646 (2007).
23. Mlodzinaski, M. J., Juette, M. F., Beane, G. L. & Bewersdorf, J. Experimental characterization of 3D localization techniques for particle-tracking and super-resolution microscopy. *Opt. Express* **17,** 8264–8277 (2009).
24. Kechkar, A., Nair, D., Heilemann, M., Choquet, D. & Sibarita, J. B. Real-time analysis and visualization for single-molecule based super-resolution microscopy. *PLoS ONE* **8,** e62918 (2013).
25. Nanguneri, S., Flottmann, B., Herrmannsdörfer, F., Kuner, T. & Heilemann, M. Single-molecule super-resolution imaging by tryptophan-quenching-induced photoswitching of phalloidin–fluorophore conjugates. *Microsc. Res. Tech.* **77,** 510–516 (2014).
26. Weber, K., Rathke, P. & Osborn, M. Cytoplasmic microtubular images in glutaraldehyde-fixed tissue culture cells by electron microscopy and by immunofluorescence microscopy. *Proc. Natl Acad. Sci. USA* **75,** 1820–1824 (1978).
27. Olivier, N., Keller, D., Rajan, V. D., Gönczy, P. & Manley, S. Simple buffers for 3D STORM microscopy. *Biomed. Opt. Express* **4,** 885–899 (2013).
28. Chizhik, A. I., Rother, J., Gregor, I., Janshoff, A. & Enderlein, J. Metal-induced energy transfer for live cell nanoscopy. *Nature Photon.* **8,** 124–127 (2014).
29. Schachter, H., Calaminus, S., Thomas, S. & Machesky, L. Podosomes in adhesion, migration, mechanosensing and matrix remodeling. *Cytoskeleton* **70,** 572–589 (2013).
30. Jungmann, R. *et al.* Multiplexed 3D cellular super-resolution imaging with DNA-PAINT and Exchange-PAINT. *Nature Methods* **11,** 313–318 (2014).
31. Tam, J., Cordier, G. A., Borbely, J. S., Alvarez, A. S. & Lakadamyali, M. Cross-talk-free multi-color STORM imaging using a single fluorophore. *PLoS ONE* **9,** e101772 (2014).
32. Valley, C. C., Liu, S., Lidke, D. S. & Lidke, K. A. Sequential superresolution imaging of multiple targets using a single fluorophore. *PLoS ONE* **10,** e0123941 (2015).
33. Wang, S., Moffitt, J. R., Dempsey, G., Xie, X. & Zhuang, X. Characterization and development of photoactivatable fluorescent proteins for single-molecule-based superresolution imaging. *Proc. Natl Acad. Sci. USA* **111,** 8452–8457 (2014).
34. Lukinavičius, G. *et al.* A near-infrared fluorophore for live-cell super-resolution microscopy of cellular proteins. *Nature Chem.* **5,** 132–139 (2013).
35. Klein, T. *et al.* Live-cell dSTORM with SNAP-tag fusion proteins. *Nature Methods* **8,** 7–9 (2011).
36. Lew, M. D., Backlund, M. P. & Moerner, W. E. Rotational mobility of single molecules affects localization accuracy in super-resolution fluorescence microscopy. *Nano Lett.* **13,** 3967–3972 (2013).

Acknowledgements

The authors thank J. Dompierre for help with immunofluorescence and P. Adenot for providing CellMask Deep Red stain. The authors acknowledge financial support from the AXA Research Fund, Labex WIFI, the French National Research Agency (project SMARTVIEW) and DIM Nano-K (Project NanoSAF).

Author contributions

N.B., G.D., E.F. and S.L.F. conceived and designed the project. N.B. performed the experiments, simulations and analysis. C.M. and N.B. developed the photoswitching buffer. C.M., N.B. and S.L. optimized the immunofluorescence protocol. T.B. and P.B. helped with the simulation and the DONALD module. All authors contributed to writing the manuscript.

Additional information

Supplementary information is available in the online version of the paper. Reprints and permissions information is available online at www.nature.com/reprints. Correspondence and requests for materials should be addressed to S.L.F.

Competing financial interests

The authors declare no competing financial interests.

Methods

Optical set-up. Three-dimensional super-localization images were acquired using a Nikon Eclipse Ti inverted microscope combined with a Perfect Focus System (Nikon) and configured for these studies with TIRF excitation. Samples were excited with 488 nm (Genesis MX-STM 500 mW, Coherent) and 637 nm (Obis 637 LX 140 mW, Coherent) optically pumped semiconductor lasers. A set of full-multiband laser filters, optimized for 405, 488, 561 and 635 nm laser sources (LF405/488/561/635-A-000, Semrock), was used to excite Alexa Fluor 488 or 647 for collection of the resultant fluorescence using a Nikon APO TIRF ×60, NA 1.49 oil immersion objective lens. All images were recorded using a 512 × 512-pixel EMCCD camera (iXon 897, Andor), split into two regions with areas of 256 × 256 pixels, and positioned at the focal plane of the DONALD module (×2.7 magnification, optical pixel size of ~100 nm).The two imaging paths were calibrated in terms of transmission efficiency to define a permanent correction factor to compensate for the imperfect beamsplitter. Fluorescent nanospheres (20 nm) deposited on a coverslip were used as a localization standard.

dSTORM imaging. To induce the majority of the fluorophores into the dark state, the samples were excited using a laser in an oblique configuration (488 nm for F-actin labelled with Alexa 488, and 647 nm for microtubules immunolabelled with Alexa 647). Once the density of fluorescent dye was sufficient (typically, less than one molecule per μm^2), we switched on the laser that was used in TIRF excitation with an irradiance of 2 kW cm^{-2} and activated the real-time three-dimensional localization performed by home-written Python code (see Supplementary Fig. 1 for more details regarding the three-dimensional localization). For all recorded images, the integration time and EMCCD gain were set to 50 ms and 150, respectively.